nature climate change

ASYMMETRIC FORCING FROM STRATOSPHERIC AEROSOLS IMPACTS SAHELIAN RAINFALL

Figure S1a shows significant inter-annual variability in seasonal SPA data with multi-decadal periods exhibiting positive and negative SPAs. A similar picture emerges when considering the N-S Atlantic SSTA (Fig S1c) although there are some differences in the exact phases of the two variables. Figure S1e shows scatter-plots of the seasonal SPA and the N-S SST anomaly. The annual-mean correlation (R=0.53) is modest with a positive slope of 38mm/K or 33%/K.

Figure S1b,d and f show the same relationships diagnosed for the model. The N–S Atlantic SSTA is reasonably represented in terms of variability (standard deviation of approximately 0.23K for observations and 0.31K for the model), but the magnitude of the SPA anomaly is rather smaller in the model than in the observations (standard deviation of approximately 16mm/month for observations and just 6mm/month for the model). This reduced magnitude of the SPA anomaly in the model is the primary reason for the reduced sensitivities of 8.6mm/K or 23%/K (R=0.43). The agreement between the model and observations is relatively better when percentage precipitation anomalies are considered because the model significantly under-predicts the absolute magnitude of Sahelian rainfall. However the clear relationship between rainfall and N-S Hemisphere SST gradients in the observations is present in the model, lending confidence to the ability of the model as a predictive tool for Sahelian precipitation changes for future scenarios.
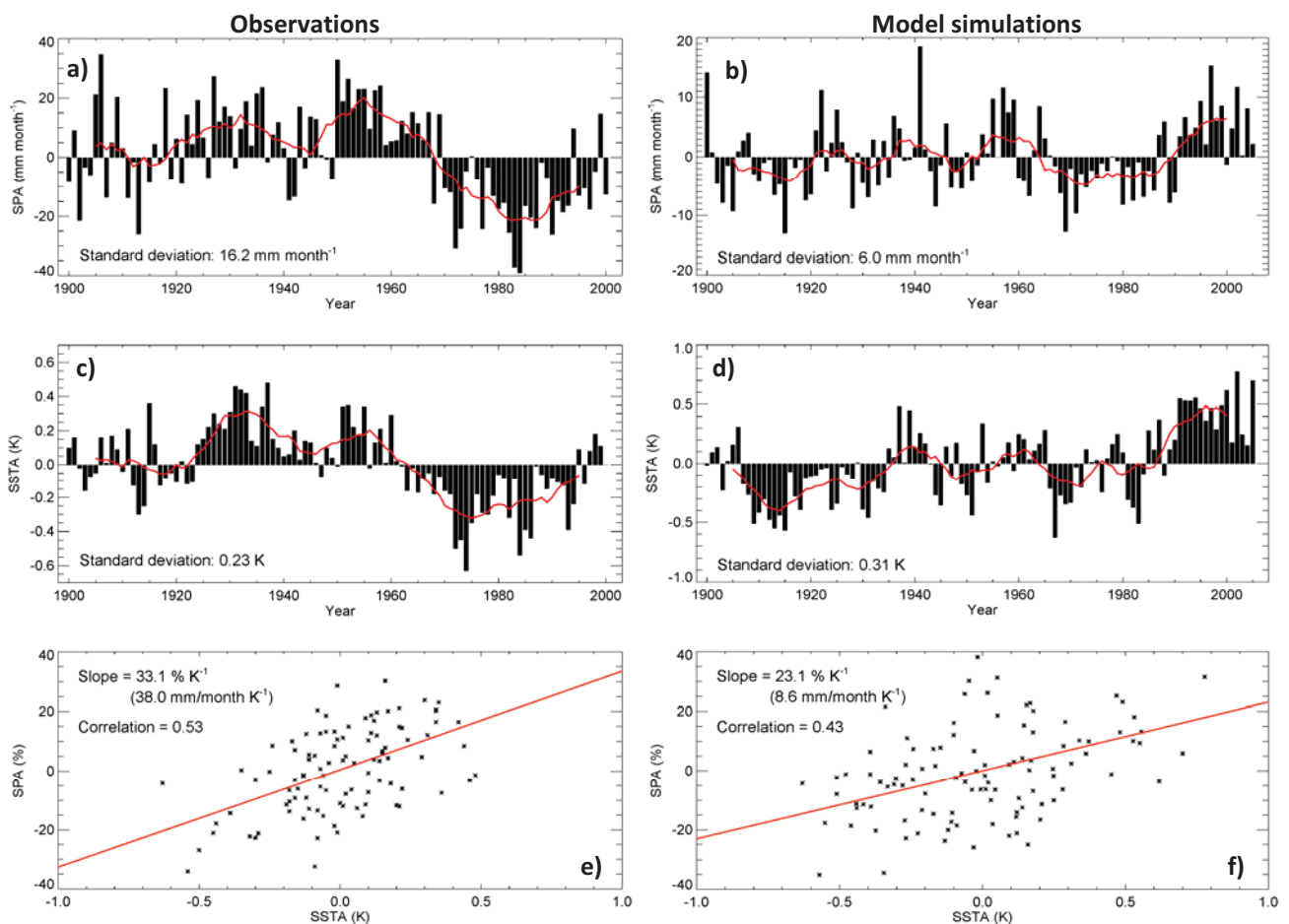

Figure S1: Time series of a) SPA from JISAO and b) SPA from HadGEM-2 model simulations, c) N–S Atlantic SSTA (K) from HADISST, d) N-S Atlantic SSTA (K) from the HadGEM-2 model simulations. In each case the red line represent the 10year running mean (10yrm). Scatter-plots of percentage SPA as a function of the N-S Atlantic SST for e) JISAO and HADISST data and f) HadGEM-2 simulations.

24 What do the patterns of precipitation anomaly responses to hemispherically symmetric volcanic
25 eruptions look like?

26 To show that the impacts on SPAs are lessened if the geographic aerosol optical depth is distributed equally
27 between the northern and southern hemispheres, the following simulations were performed. For volcanic
28 eruptions, the geographic distribution from ECNH was halved, and then an identical latitudinal distribution
29 was applied to the southern hemisphere; this simulation was called ECG where $AOD_{ECG}=(AOD_{ECNH} + $
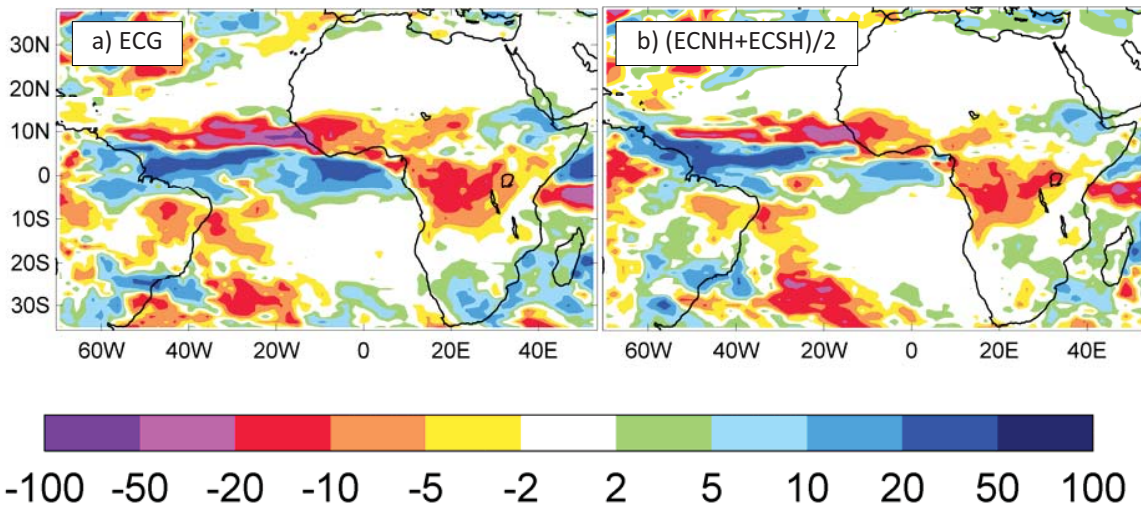30 $AOD_{ECSH})/2$.

31

32

33 Figure S2. *The change in mean precipitation (mm month^{-1}) for a) June-October for the first year of the*
34 *volcanic simulation EC4, b) June-October for the mean of the first year of the volcanic simulations*
35 *(ECNH+ECSH)/2.*

36 Figure S2a shows that to a good approximation the SPA from ECG is equivalent to the mean SPA from
37 ECNH and ECSH. Thus as the negative SPA under ECNH is stronger than the positive SPA under ECSH
38 (Figure 2), the net result is a weaker negative SPA, as evident in observations subsequent to the more
39 hemispherically symmetrical eruption of Pinatubo[S1].

40

41 **Is the timing of volcanic eruptions into the northern hemisphere important?**

42 To investigate whether a significant drought can be induced by Katmai, further simulations were performed
43 where the AODs from Katmai (eruption June 1912)[13] were used in place of those for El Chichón (eruption
44 April 1982). The spatial and temporal evolution of the SPAs are shown in Figure S3.
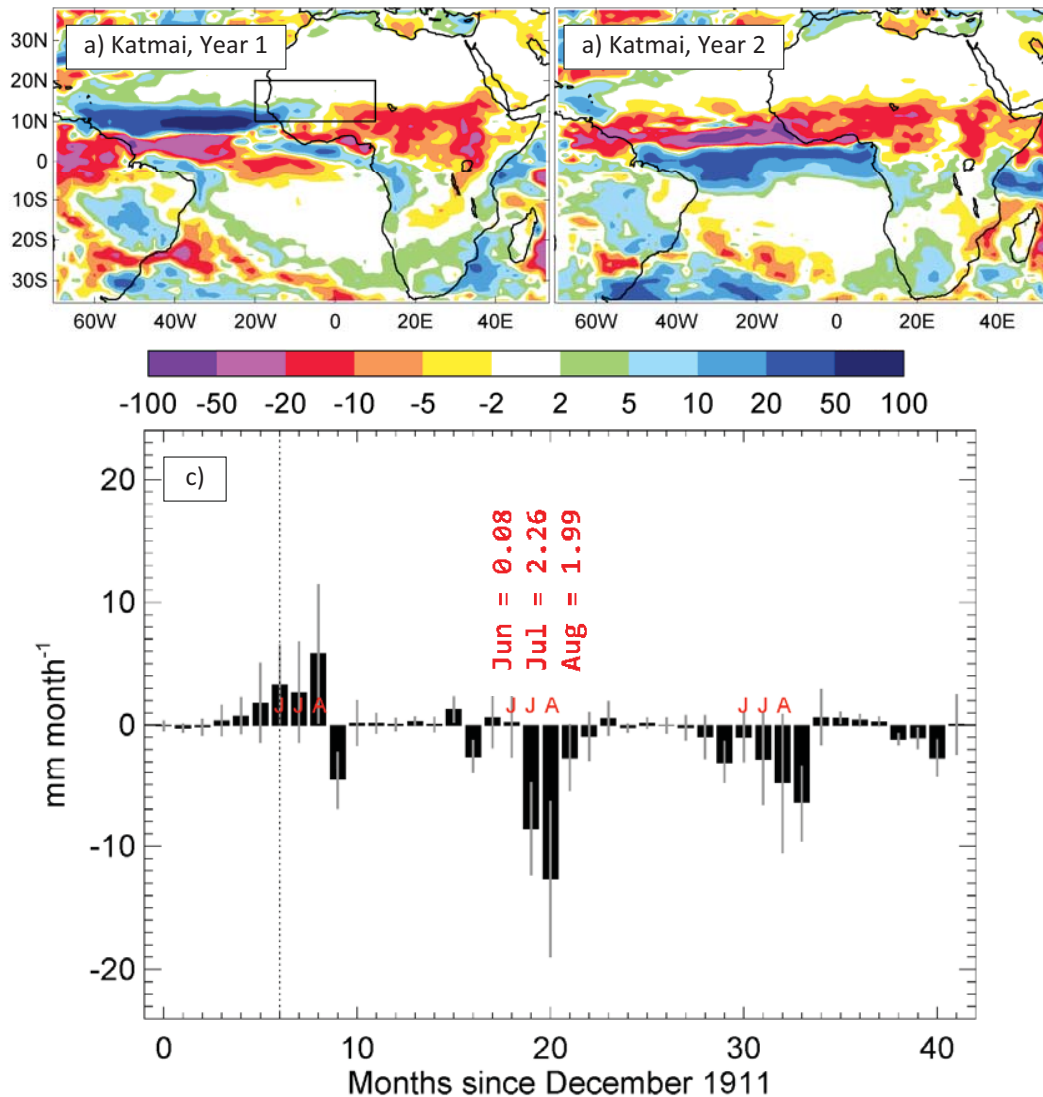
45

46

47

48 *Figure S3. The geographic distribution of difference in June-October mean precipitation (mm month⁻¹)*
49 *compared to the control simulation using means from 10-member ensembles for a) Katmai-control (year 1)*
50 *and b) Katmai-control (year 2). The geographic area 10ᵒ-20ᵒN, 20ᵒW-10ᵒE is shown by the box. The*
51 *temporal evolution of the precipitation anomalies for c) Katmai-control; the dotted line indicates the month*
52 *of the eruption in the simulations, and the whiskers represent the mean ± 1 standard deviation. The*
53 *statistical significance (in terms of the standard deviations) of the modelled SPA during June, July and*
54 *August during 1913 are shown.*

55 Figure S3 shows that there is no drought in 1912, but a statistically significant SPA (significantly different at
56 1.26 and 1.99 standard deviations) develops in 1913, a year after the eruption. This is consistent with the
57 observations and is due to the oxidation timescale of SO_2 to sulphuric acid, the dynamical timescale for
58 mixing the aerosol throughout the northern hemisphere[30] and the thermal inertia of the oceans.

59 **In the geoengineering simulations, what is the resulting global aerosol optical depth and associated**
60 **temperature change?**

61 The geographic distribution of aerosol optical depth under the G4, G4NH and G4SH simulations are shown
62 in Figures S4a-c. The temporal evolution of the global mean aerosol optical depths at 550nm is shown in
63 Figure S4d. The aerosol becomes very well mixed in the zonal direction owing to the long lifetime of aerosol
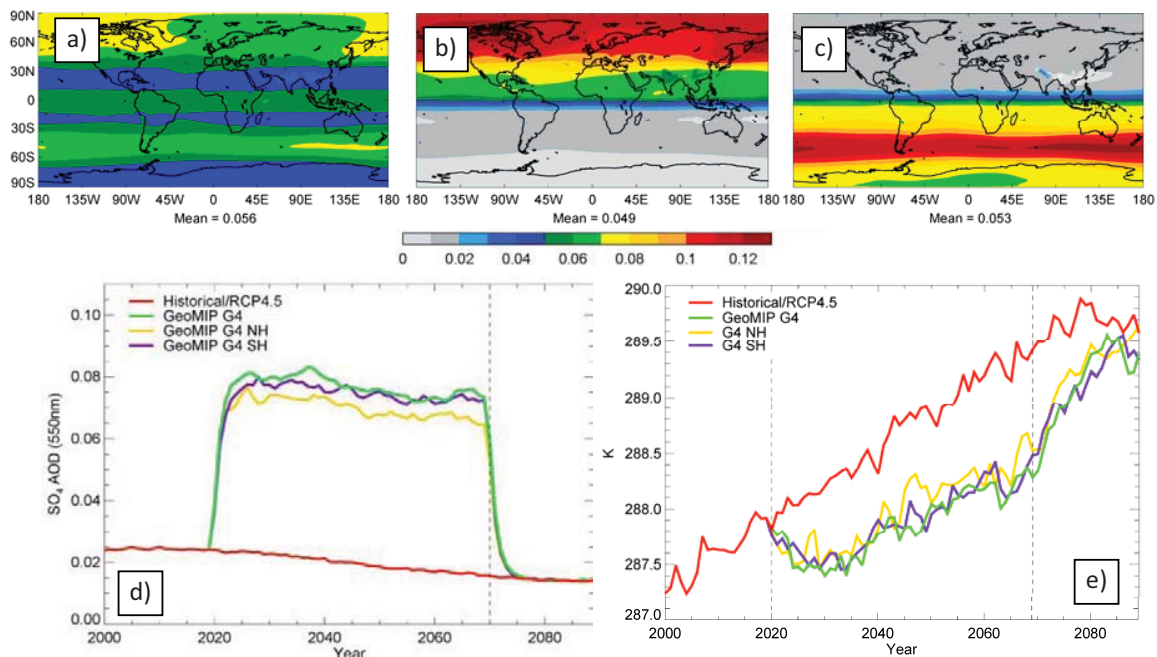**64** in the stratosphere. The global mean temperatures under the various scenarios are shown in Figure S4e.

65

66

67

68 *Figure S4. Showing the spatial distribution of the aerosol optical depths (0.55μm) under scenario*
69 *a)G4, b) G4NH, and c G4SH. d) the temporal evolution of the total sulphate aerosol optical depth*
70 *(0.55μm) from 2000 to 2090. The red line shows the levels of tropospheric sulphate associated with*
71 *the RCP4.5 simulation, e) the temporal evolution of the global annual mean near-surface air*
72 *temperature (K) from 2000 to 2090 for the RCP4.5 non-geoengineered scenario and G4, G4NH and*
73 *G4SH scenarios.*

74

75   **Is the relationship between modelled SPA and SSTA robust in the future?**

76   Figure S5 shows the SSTA associated with the RCP4.5, G4NH and GSH simulations. The SSTA for RCP4.5

77   is clearly positive during the period 2020-2070 under RCP4.5, but primarily negative during G4NH. G4SH

78   acts to strengthen the positive SSTAs that are evident in the RCP4.5 scenario.
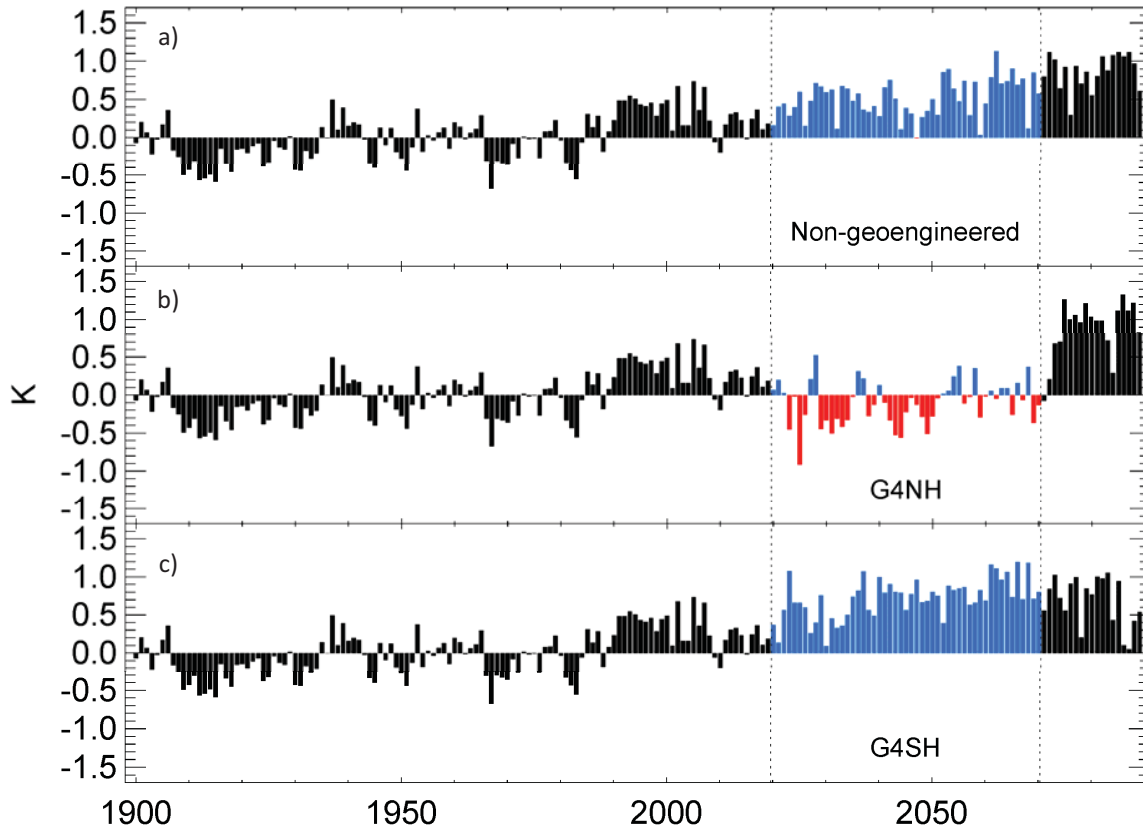
79

80   *Figure S5. The N-S Atlantic temperature anomaly (K) in HadGEM2 as a function of time. Pre-2020 the*

81   *simulations are from the CMIP5 RCP4.5 simulations while post-2020 corresponds to the a) RCP4.5, b)*

82   *G4NH and c) G4SH simulations as from 2020. The period 2020-2070 is highlighted by the red and blue*

83   *colours to emphasise the period when geoengineering occurs in b) and c)*

84

85 **What do the patterns of precipitation anomaly responses to hemispherically symmetric geoengineering**
86 **look like?**

87 A similar approach to the volcanic simulations (Figure S2) was applied for geoengineering, but using the
88 emission rates rather than AODs; following convention[21], this simulation was called G4. The resulting SPAs
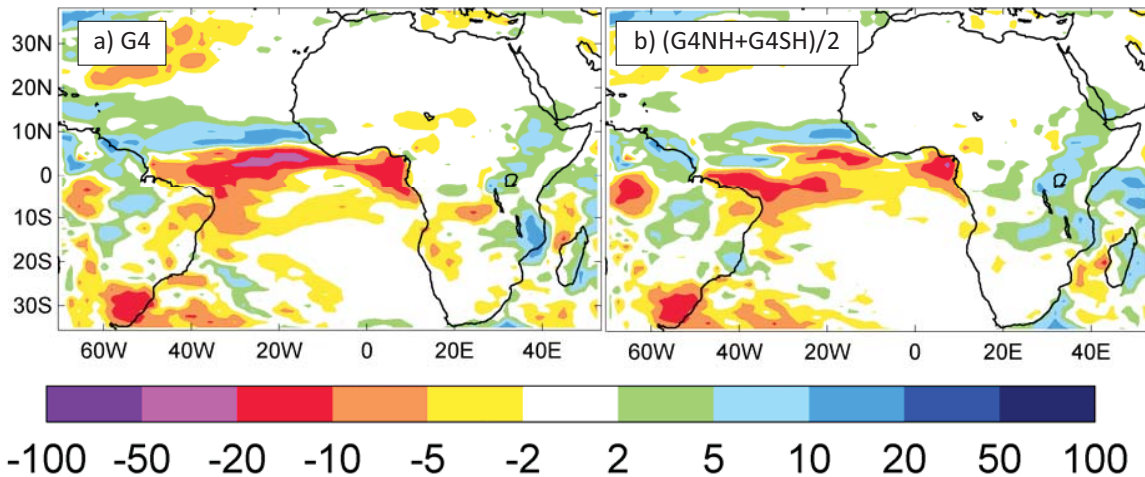89 are shown in Figure S6.

Figure S6. *The change in mean precipitation (mm month^{-1}) for the first year of the for a) annual mean for*
the 2020-2070 period of the geoengineering simulation G4 and b) annual mean for the 2020-2070 period of
the geoengineering simulation (G4NH + G4SH)/2 .

95 Figure S6 shows that to a good approximation the SPA from G4 is equivalent to the mean SPA from G4NH
96 and G4SH. Thus for both volcanic and geoengineering simulations SPA drought is most evident for
97 injections into the northern hemisphere.

98

What are the dynamical influences that drive SPA in the model?

Between 30°N-30°S the transport of moist static energy polewards from the region of maximum heating near the equator is accomplished by the overturning of the atmosphere in the Hadley Cell which consists of a rising motion near the equator, poleward transport in the upper troposphere, descent and a return flow towards the Equator at low altitudes. The Coriolis force acts to deflect the Equatorwards flow to the right in the northern hemisphere and the left in the southern hemisphere causing the easterly trade winds. This simple system is complicated by the strong interaction between deep convection, excitation of tropical waves, mesoscale systems and SST anomalies. The perturbation to the surface temperature (SST over ocean and surface skin temperature over land) for the period JJASO caused by G4NH, G4SH, ECNH and ECSH are shown in Figure S7.
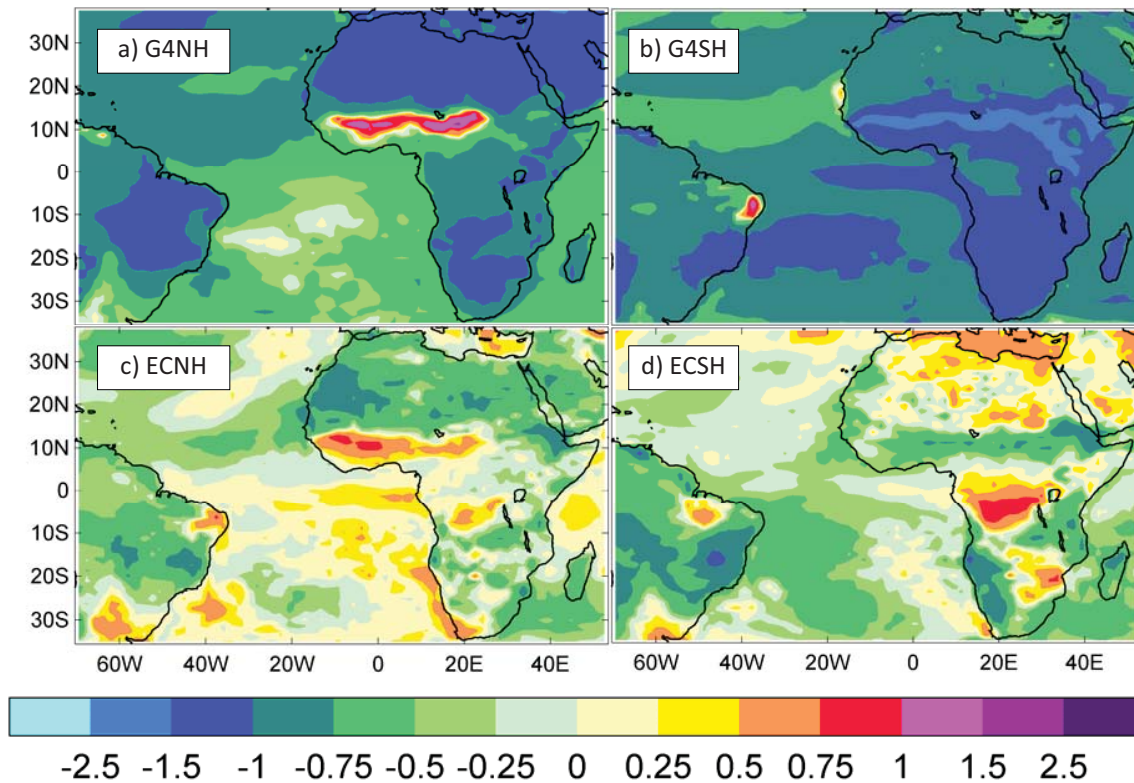

Figure S7. The mean change in June-October surface temperature (K) over the period 2020-2070 from the RCP4.5 simulation for the period caused by the a) G4NH and b) G4SH. The same quantity for the 10-member ensembles for the first year of c) ECNH, and d) ECSH scenarios.

The G4NH simulation (Figure S7a) shows a decrease in the N-S Atlantic SST gradient, and a negative SSTA which has been linked to a negative SPA anomaly in both observations and the model. G4SH (Figure S7b) shows that the southern hemisphere land and ocean cool significantly compared to the northern hemisphere linked to a positive N-S Atlantic SSTA. Figure S7a/S7b shows the strong increase/decrease in surface temperature in the Sahelian region is caused by the decrease/increase in precipitation and increase/decrease in the Bowen ratio respectively. ECNH (Figure 7c) and ECSH (Figure 7d) show relatively similar patterns in to the G4NH and G4SH simulations respectively, but the magnitude of the cooling is less owing to the transient nature of the volcanic forcing when compared to that for geoengineering. The timescale of the forcing is sufficient to cause both hemispheres to cool in the geoengineering simulations owing to inter-hemispheric heat transfer in ocean circulations, but only the northern hemisphere to cool under ECNH and only the southern hemisphere to cool under ECSH.

126 We plot the mean meridional vertical streamfunction from the RCP4.5 simulation to diagnose the
127 overturning circulation pattern over the Atlantic regions for longitude band 60°W-20°E together with the
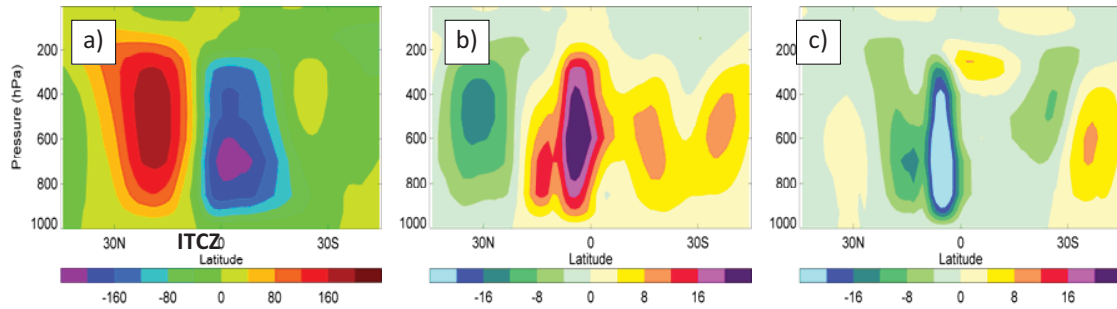128 anomalies under G4, G4NH and G4SH scenarios.

129

130 *Figure S8. a) Mean meridional vertical streamfunction **ψ** (kg/ms⁻¹) (2020-2070) diagnosed for June-October*
131 *under the non-geoengineered RCP4.5 simulation for the Africa/Atlantic region bounded by 45N-45S,*
132 *60W-20E. Positive values represent anti-clockwise rotation while negative values represent clockwise*
133 *rotation. Change in **ψ** from the RCP4.5 simulation for b) G4NH and c) G4SH.*

134

135 Figure S8a shows the expected meridional overturning with the ITCZ located at the interface between the
136 northern hemisphere and the southern hemisphere branches of the Hadley circulation being located at around
137 8°N as annotated. The change in **ψ** between G4 and RCP4.5 is relatively minor, and will not be discussed
138 further. The impact of G4NH is to reduce maximum SST and displace it to the south hence reducing the
139 strength of the circulation in both the northern and southern branches of the Hadley Cell and displaces it to
140 the south (Figure S8b). Figure S8c shows that the impact of G4SH is to invigorate the southern branch of the
141 Hadley Cell and displace the ITCZ to the north.

142 Given that the large scale Hadley circulation appears to be perturbed, we next look in more detail at the
143 mesoscale impact on the monsoon circulation. In Figure S9, we plot the low level 950hPa moisture flux[3],
144 which is the specific humidity multiplied by the horizontal component of the wind vector and has units of
145 kgkg⁻¹ms⁻¹. We also show the precipitation in mmday⁻¹ in the coloured contours.

146

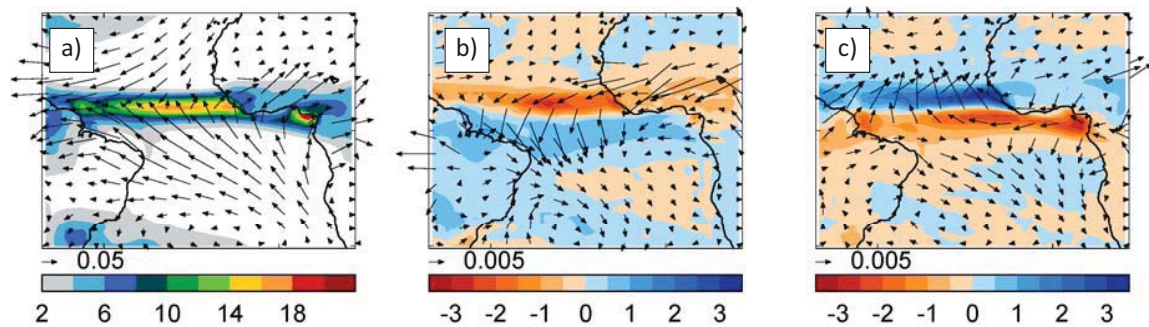147 *Figure S9. Showing a) the precipitation (mmday⁻¹) in the coloured contours and the 950hPa moisture flux*
148 *(kgkg⁻¹ms⁻¹) in arrows associated with the RCP4.5 scenario averaged over the June-October monsoon*
149 *season for the period 2020-2070 (inclusive). The perturbation to these fields for b) G4NH and c) G4SH.*

150 Figure S9a shows that over oceans, convergence of the two branches of the Hadley Cell are evident with
151 Easterly trade winds being clearly visible. Convergence of the 950hPa moisture flux is clearly associated
152 clearly with the intense areas of precipitation over ocean regions in the model. The African monsoon flow
153 consists of low-level moisture transfer from the Gulf of Guinea to the interior of the African continent[3].
154 Figure S9b represents the perturbation from the G4NH simulation and the opposition to the monsoon flow of
155 moisture into the interior of the African continent is very evident particularly at the northern extreme of the

156   monsoon flow thereby weakening precipitation. Figure S9c shows the impact of G4SH. The moisture flow
157   generally acts to enhance the monsoon flow rather than oppose it, leading to an increase in moisture transport
158   to the interior of the continent and enhanced precipitation.

159   [S1] Trenberth, K. E., and A. Dai, 2007, Effects of Mount Pinatubo volcanic eruption on the hydrological cycle as an analog of geoengineering,
160   Geophys. Res. Lett., 34, L15702, doi:10.1029/2007GL030524.
161
162